Magnetohydrodynamic simulations of the elliptical instability in triaxial ellipsoids

David Cébron, Michael Le Bars, Pierre Maubert, Patrice Le Gal

▶ **To cite this version:**

David Cébron, Michael Le Bars, Pierre Maubert, Patrice Le Gal. Magnetohydrodynamic simulations of the elliptical instability in triaxial ellipsoids. Geophysical and Astrophysical Fluid Dynamics, 2012, 106 (4-5), pp.524-546. 10.1080/03091929.2011.641961 . hal-00859372

HAL Id: hal-00859372
https://hal.science/hal-00859372

Submitted on 7 Sep 2013

HAL is a multi-disciplinary open access archive for the deposit and dissemination of scientific research documents, whether they are published or not. The documents may come from teaching and research institutions in France or abroad, or from public or private research centers.

L'archive ouverte pluridisciplinaire **HAL**, est destinée au dépôt et à la diffusion de documents scientifiques de niveau recherche, publiés ou non, émanant des établissements d'enseignement et de recherche français ou étrangers, des laboratoires publics ou privés.

Geophysical and Astrophysical Fluid Dynamics
Vol. 00, No. 00, Month 200x, 1–19

Magnetohydrodynamic simulations of the elliptical instability in triaxial ellipsoids

D. Cébron, M. Le Bars, P. Maubert and P. Le Gal

Aix-Marseille Univ., IRPHE (UMR 6594), 13384, Marseille cedex 13, France.

(*received xxx*)

The elliptical instability can take place in planetary cores and stars elliptically deformed by gravitational effects, where it generates large-scale three-dimensional flows assumed to be dynamo capable. In this work, we present the first magneto-hydrodynamic numerical simulations of such flows, using a finite-element method. We first validate our numerical approach by comparison with kinematic and dynamic dynamos benchmarks of the literature. We then systematically study the magnetic field induced by various modes of the elliptical instability from an imposed external field in a triaxial ellipsoidal geometry, relevant in a geo- and astrophysical context. Finally, in tidal induction cases, the external magnetic field is suddenly shut down and the decay rates of the magnetic field are systematically reported.

1 Introduction

Many celestial bodies (planets, stars, galaxies...) possess their own magnetic field, either by induction from an external field, or by a natural dynamo mechanism. Up to now, only two kinds of natural forcing have been identified as dynamo-capable in celestial bodies: (i) thermo-solutal convection (Glatzmaier and Roberts 1995), which is the standard mechanism generally applied to all planetary configurations even if it is not proved to be always relevant; and (ii) precession (Tilgner 2005), a purely mechanical forcing that may drive dynamos in some planets and moons (Malkus 1968), despite a well-known controversy on its energetic budget (see Rochester et al. 1975, Loper 1975 for critisms of this hypothesis, and Kerswell 1996 for its rehabilitation). On Earth today, the magnetic field is very likely generated by thermochemical convective motions within the electrically conducting liquid core, driven by the solidification of its inner core. However, the origin of the magnetic field in the Early Earth, in the Moon, in Ganymede or in Mars is more uncertain, and leads to the consideration of alternative dynamo mechanisms (Jones 2003, 2011). The recent discovery of fast magnetic reversals on the extra-solar star Tau-boo (Donati et al. 2008, Fares et al. 2009), which may be related to strong tidal effects due to the presence of a massive close companion (Fares et al. 2009), also requires to re-evaluate classical models of convective dynamos. Indeed, even when the dynamo is of a convective origin, the role of other driving mechanisms can be very important in the organization of fluid motions.

In addition to convection and precession, two other mechanisms have also been proposed to be of fundamental importance to drive cores flows, and consequently to influence planetary magnetic fields: libration and tides. As recently shown in Cébron et al. (2011), both these forcings are indeed capable of extracting huge amount of rotational energy to create complex three-dimensional motions through the excitation of a so-called elliptical instability, also called tidal instability in the astrophysical context. The elliptical instability is a generic instability that affects any rotating fluid whose streamlines are elliptically deformed (see for instance the review by Kerswell 2002). A fully three-dimensional turbulent flow is excited in the bulk as soon as (i) the ratio between the ellipticity β of the streamlines and the square root of the Ekman number E is larger than a critical value of order one and (ii) a difference in angular velocity exists between the mean rotation of the fluid and the elliptical distortion. In a planetary context, the ellipticity of

* Corresponding author. Email: cebron@irphe.univ-mrs.fr

Geophysical and Astrophysical Fluid Dynamics
ISSN 0309-1929 print/ ISSN 1029-0419 online ©2006 Taylor & Francis Ltd
http://www.tandf.co.uk/journals
DOI:10.1080/03091920xxxxxxxxx

Geophysical and Astrophysical Fluid Dynamics
ISSN: 0309-1929 print/ISSN 1029-0419 online © 200x Taylor & Francis
DOI: 10.1080/03091920xxxxxxxxx

streamlines is related to the tidal deformation of the planetary layers. A differential rotation is generically present between the core fluid and the dynamic tides in non-synchronized systems; it also appears between the static bulge and the core fluid because of librations in synchronized ones. The elliptical instability is then refereed to tide driven elliptical instability (TDEI) and libration driven elliptical instability (LDEI), respectively.

So far, magneto-hydrodynamic (MHD) simulations of stellar or planetary flows have been performed in spherical, and recently spheroidal (i.e. axisymetric around the rotation axis), geometries, which facilitate and accelerate the computations but also prevent the growth of any elliptical instability. Because of the small amplitudes of tidal bulges, this approximation could be thought to be correct. But since the elliptical instability comes from a parametric resonance, even an infinitesimal deformation can lead to first order modifications of the flow (Lacaze et al. 2004, Cébron et al. 2010a). To study its MHD consequences, we have thus developed the first numerical MHD simulations in a triaxial ellipsoidal geometry, which are presented below.

The paper is organized as follows. In section 2, the numerical method used to solve MHD flows in a non-axisymmetric geometry is described. In section 3, validations of our method are presented, considering kinematic dynamos with different mesh elements and boundary conditions, but also a thermally driven dynamic dynamo following the standard benchmark proposed by Christensen et al. (2001). In section 4, the code is finally used to study induction processes by the elliptical instability. These simulations are then used to systematically study the decay rates of the magnetic field when the external magnetic field is suddenly shut down.

2 Numerical model

2.1 *Local methods in MHD simulations*

Since the pioneering work of Glatzmaier and Roberts (1995), numerical simulations have more and more deeply studied how a convective dynamo process can generate a magnetic field in a rotating shell. Many comparisons with the observational data, mainly obtained on Earth but also on other planets of the solar system, have been done to confirm the relevance of these simulations (e.g. Dormy et al. 2000, for a review). Some key features like the dipole dominance, the westward drift and the occasional reversals of the magnetic field, are recovered by various codes. However, due to computational costs, the dimensionless parameters used in numerical simulations are very different from the realistic values of planetary cores (Busse 2002). To get as close as possible to the real parameter values, the numerical codes are optimized and massively parallel. Usually, numerical simulations of magneto-hydrodynamic flows in planetary cores benefit from their spherical geometry to use fast and precise spectral methods. However, since global communication is required (e.g. Clune et al. 1997), such methods are difficult to parallelize. Following the precursory work of Kageyama and Sato (1997), some studies have been performed using local methods, more easily adapted to parallel architectures, and thus more suitable for massively parallel computations: see for instance the works of Chan et al. (2001), Matsui and Okuda (2004, 2005) using finite-element methods; the works of Hejda and Reshetnyak (2003, 2004), Harder and Hansen (2005) using finite-volume methods; and the work of Fournier et al. (2004, 2005) using spectral elements. Besides, even if all these previous studies have been performed in spheres, local methods also have the great advantage of providing robust and accurate solutions for arbitrary geometries, which is of direct interest for our study of flows driven in triaxial ellipsoidal geometries.

2.2 *MHD equations*

We consider a finite volume of conducting fluid of kinematic viscosity ν, density ρ, magnetic diffusivity ν_m and electrical conductivity γ, rotating with a typical rate Ω and enclosed in a rigid container of typical size R. Using R as a lengthscale, Ω^{-1} as a time scale, and $\Omega\ R\sqrt{\rho\mu_0}$ as a magnetic field scale, where μ_0 is the vacuum magnetic permeability, the magnetohydrodynamics equations in the non-relativistic limit

(equivalently, considering only timescales greater than the relaxation time of the charge carriers) write

$$\frac{\partial \mathbf{u}}{\partial t} + \mathbf{u}\cdot\nabla\mathbf{u} = -\nabla p + E\,\triangle\,\mathbf{u} - 2\,\boldsymbol{\Omega}\times\boldsymbol{u} + (\nabla\times\mathbf{B})\times\mathbf{B_{tot}}, \tag{1}$$

$$\nabla\cdot\mathbf{u} = 0, \tag{2}$$

$$\frac{\partial \mathbf{B}}{\partial t} = \nabla\times(\mathbf{u}\times\mathbf{B_{tot}}) + \frac{1}{Rm}\,\triangle\,\mathbf{B}, \tag{3}$$

$$\nabla\cdot\mathbf{B} = 0. \tag{4}$$

where $(\mathbf{u}, p, \mathbf{B})$ are respectively the velocity, pressure and magnetic fields, and $\mathbf{B_{tot}} = \mathbf{B} + \mathbf{B_0}$ is the total magnetic field accounting for a possible constant and uniform $\mathbf{B_0}$, representing the imposed external magnetic field in induction problems. The right-hand side term $(\nabla\times\mathbf{B})\times\mathbf{B_{tot}}$ in equation (1) corresponds to the so-called Laplace (or Lorentz) force. Dimensionless numbers are the Ekman number $E = \nu/(\Omega\,R^2)$, and the magnetic Reynolds number $Rm = Pm/E$, where $Pm = \nu/\nu_m$ is the magnetic Prandtl number. In this work, the no-slip boundary condition is systematically used for the fluid. Note that a Coriolis force $-2\,\boldsymbol{\Omega}\times\boldsymbol{u}$, where $\boldsymbol{\Omega}$ is the rotation vector of the working frame of reference, is introduced here for generality and will be used in section 3.3. Once the magnetic field is solved, the Maxwell's system of equations allows us to deduce the current density $\mathbf{j} = \nabla\times\mathbf{B}/\mu_0$, the electric potential $\triangle V_e = \nabla\cdot(\mathbf{u}\times\mathbf{B})$ and the charges distribution $\rho_e = -\epsilon\nabla\cdot(\mathbf{u}\times\mathbf{B})$, where ϵ is the electric permittivity of the fluid.

Usually, numerical simulations of magneto-hydrodynamic flows in planetary cores benefit from their spherical geometry to use fast and precise spectral methods. In our case however, we do not consider any simple symmetry. Our computations are thus performed with a standard finite-element method, widely used in engineering studies, which allows to deal with complex geometries and to simply impose the fluid boundary conditions. However, solving the magnetic field with local methods gives rise to some difficulties that we have to cope with. In the finite-element community, the MHD simulations are usually done with a formulation in terms of magnetic potential vector defined by $\mathbf{B} = \nabla\times\mathbf{A}$ (see e.g. Matsui and Okuda 2005), which ensures that the field remains divergence free at any time. Equations (3-4) are thus replaced by

$$\frac{\partial \mathbf{A}}{\partial t} = (\mathbf{u}\times\mathbf{B_{tot}}) + \frac{1}{Rm}\,\triangle\,\mathbf{A}, \tag{5}$$

$$\mathbf{B_{tot}} = \nabla\times\mathbf{A} + \mathbf{B_0} = \mathbf{B} + \mathbf{B_0}. \tag{6}$$

Naturally, the two MHD equations (3-4) can be recovered from equations (5-6). The absence of gauge, usually introduced in potential vector formulation (e.g. Matsui and Okuda 2005), prevents us from dealing with purely insulating domain. Indeed, in such domains, the electric field is the Lagrange multiplier associated with the constraint $\boldsymbol{\nabla}\times\boldsymbol{B} = \mathbf{0}$ (e.g. Guermond et al. 2007). This imposes to use a supplementary variable ϕ, which is a Lagrange multiplier to ensure the gauge $\nabla\cdot\mathbf{A} = 0$. The variable ϕ is equivalent to the pressure p for the velocity field. Consequently, since we do not impose any gauge, we cannot use perfectly insulating materials in the following. Thus, we model them by very weakly conducting domains compared to the metallic ones.

2.3 *Boundary conditions*

The non-local nature of the magnetic boundary conditions is a long-standing issue in dynamo modeling. Usually with spectral methods, the matching of the magnetic induction at the boundaries with an outer potential field is easily tractable. However, using local methods, a main issue remains regarding the conflict between local discretization and the global form of the magnetic boundary conditions. As reviewed in Iskakov et al. (2004), different solutions have been proposed in the literature to cope with this problem. The so-called quasi-vacuum condition $\mathbf{n}\times\mathbf{B} = \mathbf{0}$ ($\mathbf{n}$ being the local normal vector), which is a local condition representing for instance an outside domain made of a perfect 'magnetic conductor' ($\mu\to\infty$), has been

used by Kageyama and Sato (1997) and Harder and Hansen (2005). The immersion of the bounded domain into a large domain where the magnetic problem is also solved has been used by Chan et al. (2001) and improved by Matsui and Okuda (2004) in using the potential vector. The combination of the local method with an integral boundary elements method (BEM) has been introduced by Iskakov et al. (2004) by coupling a finite volume method with the BEM. Here, following Matsui and Okuda (2004), we choose solutions (i) or (ii), depending on the considered problem. When the solution (ii) is used, we impose on a distant external spherical boundary the magnetic condition $\mathbf{A} \times \mathbf{n} = \mathbf{0}$, which corresponds to $\mathbf{B} \cdot \mathbf{n} = 0$.

2.4 *Numerical method*

To solve the complete MHD problem, we use the commercial software COMSOL Multiphysics®. For the fluid variables, the mesh element type is the standard Lagrange element $P1 - P2$, which is linear for the pressure field and quadratic for the velocity field. Note that higher order elements such as $P2 - P3$ would have a better convergence rate with the number of mesh elements but would impose a significant supplementary computational cost. For a given computational cost, the use of $P1 - P2$ elements allows to use a finer mesh.

Lagrange elements are nodal elements, well adapted to solve for the velocity field. However, as reminded by Hesthaven and Warburton (2004), the use of this kind of elements in a straightforward nodal continuous Galerkin finite-element method is known to lead to the appearance of spurious, non-physical solutions (e.g. Sun et al. 1995, Jiang et al. 1996, for a review). Their origin has several interpretations such as a poor representation of the large null space of the involved operator (e.g. Bossavit 1988) or the generation of solutions that violate the divergence conditions, which are typically not imposed directly (Paulsen and Lynch 1991). Another difficulty is that the singular component of the solution may be not computed if the interface between a conductive medium and a non-conductive medium is not smooth (see the lemma of Costabel et al. 1991). Finally, difficulties appear on the coupling of fields across such an interface. A first way to overcome these difficulties is to use specific method such as interior penalty discontinuous Galerkin methods (e.g. Guermond et al. 2007, for MHD applications). A second way to solve this problem is to construct elements adapted to the operator. In a pionnering work, Bossavit (1988, 1990) shows that the use of special curl-conforming elements (Nédélec 1980, 1986) allows to overcome the problem of spurious modes. Finite-element methods based on such curl-conforming elements, also called Nédélec's edge (or vector) elements, constitute now the dominating approach for solving geometrically complex problems (e.g. Jin 1993, Volakis et al. 1998). An important advantage of edge elements is that they ensure the continuity of tangential field components across an interface between different media, while leaving the normal field components free to jump across such interfaces, which is a typical property of electromagnetic problems (see also Monk 2003, for details). This also implies that the curl of the vector field is an integrable function, so these elements are suitable for equations using the curl of the vector field, such as the potential vector.

In this work, the mesh element type employed for the magnetic potential vector is thus the Nédélec edge element, either linear or quadratic depending on the considered problem. The number of degrees of freedom (DoF) used in most simulations of this work ranges between $5 \cdot 10^4$ DoF for kinematic dynamos and $8 \cdot 10^5$ DoF for full MHD problems with a magnetic Reynolds number about 10^3. We use the so-called Implicit Differential-Algebraic solver (IDA solver), based on backward differencing formulas (see Hindmarsh et al. 2005 for details on the IDA solver). The integration method in IDA is variable-order (and variable-coefficient BDF), the order ranging between 1 and 5. At each time step the system is solved with the sparse direct linear solver PARDISO (www.pardiso-project.org). Up to know, the commercial software COMSOL Multiphysics® was not parallelized, and all computations were performed on a single workstation with 96 Go RAM, and two processors Intel® Xeon® E5520 (2.26 GHz, 8MB Cache). Note that each numerical simulation presented in this work typically requires 64 Go RAM and was performed on a single processor, which leads to typical CPU times of half a day for kinematic dynamos and induction calculations and CPU time of weeks when the full dynamo problem is solved. Note also that the latest version of COMSOL Multiphysics® delivered in the summer 2011 should allow parallelized calculations and we hope to access to a significantly increased numerical power very soon. In addition to their purely

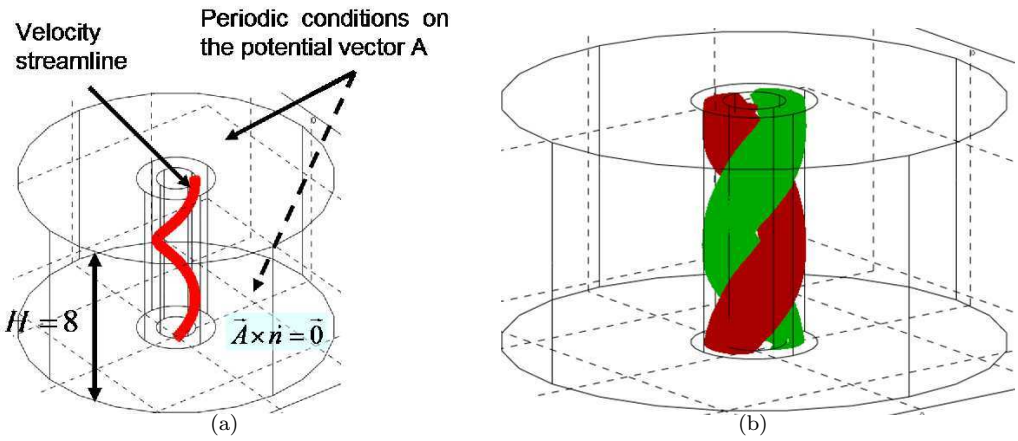

Figure 1. (a) Sketch of the Ponomarenko-like problem solved in the numerical simulations. In the region $r \leq 1$, the helical flow (7) is imposed; in the region $r \in [1;2]$, the fluid is supposed at rest; and the region $r \in [2;8]$ is assumed to be insulating. (b) Iso-surfaces of the axial component of the magnetic field with 25 % of the maximum (red) and 25 % of the minimum (green) determined with our code at $R_m = 20$.

.

scientific interest, results presented in this paper should thus be considered as a first step towards solving MHD numerical problems with this commercial software.

3 Validation of the model

3.1 *Ponomarenko-like dynamo problem*

We consider in this section a Ponomarenko-like configuration, which is a well-known kinematic dynamo. In his original formulation, Ponomarenko (1973) considered the flow of an electrically conductive fluid within a cylinder of radius R, immersed into an infinite conductive medium at rest. The flow is a solid body screw motion, defined in cylindrical coordinates (r, θ, z) by

$$\mathbf{u} = \begin{bmatrix} u_r \\ u_\theta \\ u_z \end{bmatrix} = \begin{bmatrix} 0 \\ \Omega\, r \\ R_b\, \Omega R \end{bmatrix}, \tag{7}$$

where R_b is the ratio between the axial velocity and the rotation velocity at the boundary $r = R$, i.e. the pitch of the spiral. We choose R and Ω^{-1} as the lengthscale and the timescale, respectively. With this imposed flow, the kinematic dynamo problem is analytically tractable and the critical eigenmode associated to the smallest magnetic Reynolds number $R_m^c = 17.73$ corresponds to $R_b = 1.3$, $k = -0.39$ and $m = 1$, where k and m are respectively the axial and azimuthal wavenumbers of the solution.

As sketched in figure 1a, we consider the slightly different case of an helical flow immersed into a stagnant conductive medium with the same electrical conductivity in the region $r \in [1;2]$, and an insulating region $2 \leq r \leq 8$. We use $R_b = 1$ and a height $H = 8$, similar to Kaiser and Tilgner (1999), Laguerre (2006). The boundary conditions are $\mathbf{A} \times \mathbf{n} = \mathbf{0}$ on the outer sidewall, and we impose periodicity of the potential vector on the top/bottom of the cylinder. As explained in section 2.2, the insulating domain $2 \leq r \leq 8$ is replaced in our code by a domain 10^{-8} times less conductive than the fluid domain. Concerning the validation of the numerical code, the interest of this problem is threefold: comparing our results with thoses of the literature, we can estimate (i) the influence of the non-zero outer conductivity, (ii) the capacity of the code to solve discontinuities of the flow and of the electrical conductivity, and (iii) the relevance of our boundary conditions.

A typical result of the magnetic field excited above the dynamo threshold is shown in figure 1b. This structure is in perfect agreement with the expected field (see e.g. Laguerre 2006). To study more precisely the dynamo threshold, we consider the temporal evolution of the dimensionless quadratic mean magnetic

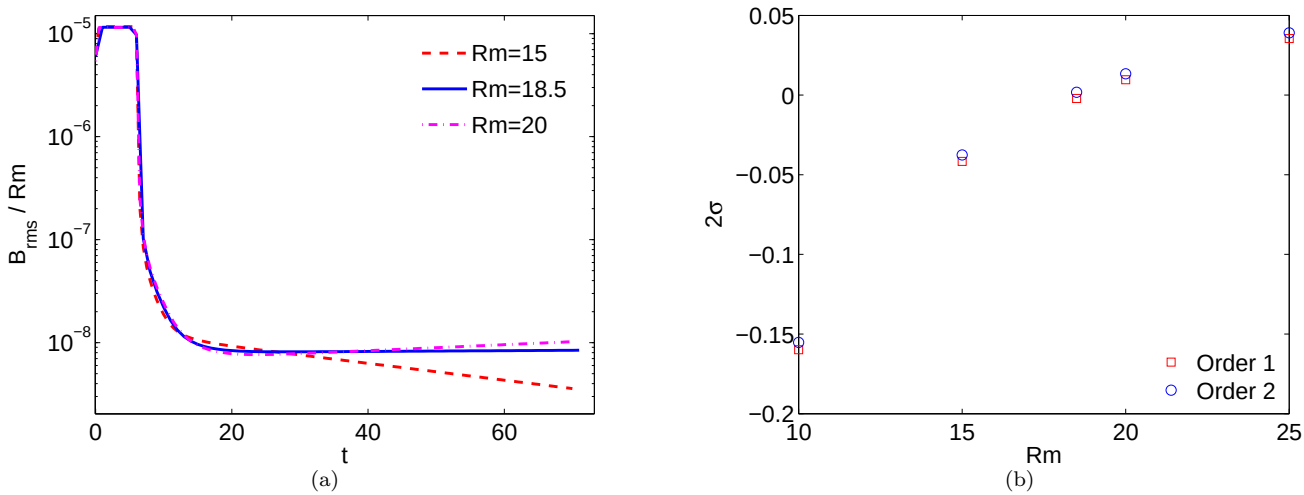

Figure 2. Numerical results for the Ponomarenko-like kinematic dynamo. (a) Temporal evolution of the quadratic mean magnetic field divided by the magnetic Reynolds number, below the dynamo threshold ($Rm = 15$), around the threshold ($Rm = 18.5$) and above the threshold ($Rm = 20$), using quadratic edge elements. (b) Evolution of the growth rate of the dynamo with the magnetic Reynolds number using linear and quadratic Nedelec elements. The mesh is the same in both cases, with 43 162 tetrahedral elements, but the order of the elements leads to a model with 52239 DoF using linear edge element, and 279560 DoF using quadratic edge elements.

field strength

$$B_{rms} = \sqrt{\frac{1}{V_s}\int_{V_s} B^2 \, \mathrm{d}V}, \tag{8}$$

where V_s is the volume of the cylinder of radius 1 non-dimensionalized by R^3. Three examples are shown in figure 2a, respectively below, above and at the dynamo threshold. The growth/decay rate σ of the magnetic field shown in figure 2b, is deduced from the growth/decay rate σ of B_{rms}, determined from the exponential fit of its temporal evolution. The threshold is precisely found at $Rm_c \approx 18.3$, in excellent agreement with the threshold of $Rm_c \approx 18.5$ found by Laguerre (2006). Note that in this case, the order of the edge (Nédélec) elements used to compute the magnetic field does not really matter.

3.2 *Von Karman kinematic dynamo: test of the ferromagnetic boundary conditions*

To test the quasi-vacuum boundary condition $\boldsymbol{n} \times \boldsymbol{B} = \boldsymbol{0}$, we consider a Von Karman kinematic dynamo in a cylinder of radius R and of aspect ratio $H/R = 2$. The dimensionless base flow is given in Gissinger (2009)

$$\boldsymbol{U} = \begin{bmatrix} U_r \\ U_\theta \\ U_z \end{bmatrix} = \begin{bmatrix} -\dfrac{\pi}{2}\, r\, (1-r)^2\, (1+2\,r)\cos(\pi z) \\ \dfrac{8}{\pi}\, r\, (1-r)\, \arcsin(z) \\ (1-r)(1+r-5\,r^2)\, \sin(\pi z) \end{bmatrix} \tag{9}$$

Following Gissinger (2009), we define here the magnetic Reynolds number by $Rm = U_{max}\, R/\nu_m$, with U_{max} the peak velocity of the mean flow. In figure 3a, the magnetic field and the base flow (9) are shown. As expected, the magnetic field induced by this flow is an equatorial dipole (e.g. Gissinger 2009). On the contrary, note that the magnetic field observed in the Von-Karman Sodium experimental dynamo is an axial dipole, which has been attributed to the non-axisymmetric component of the flow (Gissinger 2009). In figure 3b, the growth/decay rate σ for different meshes and orders of elements are shown. With the second order elements, the results are converged, and we find a critical magnetic Reynolds number

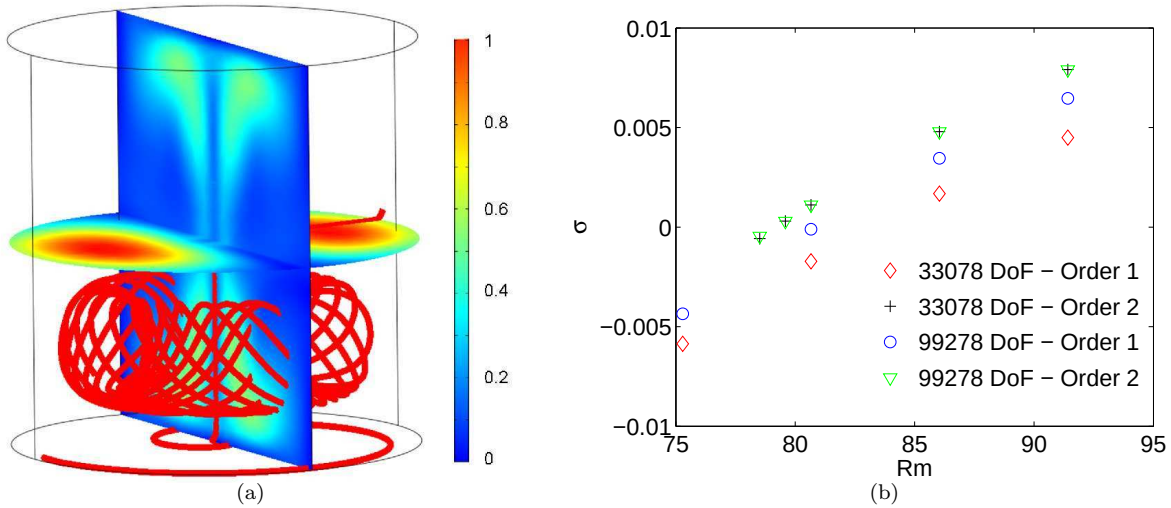

(a) (b)

Figure 3. Numerical results for the Von Karman kinematic dynamo using ferromagnetic boundary conditions. (a) Considering a simulation above the dynamo threshold ($Rm = 80.6$, 99278 DoF, using quadratic vector elements), the norm of the magnetic field (normalized by its maximum value) during its exponential growth is represented on slices. Streamlines of the velocity field used, given by (9), are also shown (only in the lower half of the cylinder). (b) The evolution of the growth/decay rate σ of the kinematic dynamo is represented as a function of the magnetic Reynolds number for two different meshes, with the linear or the quadratic edge elements. The threshold value $Rm_c = 79$ is obtained by interpolation.

$Rm_c = 79.2$ with $U_{max} = 1.0755$, reached in $(r, z) = (0.4842, \pm 1)$, which is in very good agreement with the threshold value $Rm_c = 79$ found numerically by C. Nore and A. Giesecke using two other codes (private communications). On the other hand, this threshold differs significantly from the value $Rm = 60$ given by Gissinger (2009). Figure 3b shows also that the order of elements has an influence with this kind of boundary conditions even if the values obtained are close to each others. Actually, a closer look on the magnetic field at the boundary shows that the boundary conditions are much more respected with the second order elements than with the first order ones. Anyway, this validation case shows that the code is able to reproduce correctly ferromagnetic conditions.

3.3 *Thermal convection dynamo benchmark*

As shown in the previous sections, our numerical approach is able to study kinematic dynamos. The present section extends the validation to dynamic dynamos considering the usual numerical benchmark of Christensen et al. (2001) driven by thermal convection in a rotating sphere. Up to now, this benchmark, initially defined with spectral methods, has only been considered in two works using local numerical methods: Matsui and Okuda (2004, 2005) reproduced the benchmark on the Earth Simulator with a finite element method based on a potential formulation; Harder and Hansen (2005) used a finite volume method and consider a slighty different case, using pseudo-vaccum conditions at the external boundary. In the present work, we consider the case of Harder and Hansen (2005), using our commercial software, based on vector elements.

We thus solve also the energy equation and add a buoyancy force in the Navier Stokes equations, as already shown in Cébron et al. (2010b). The Boussinesq approximation is used and gravity varies linearly with radius. For direct comparison, we use here the scaling of Christensen et al. (2001). The considered geometry corresponds to a rotating spherical shell of aspect ratio $\eta = 0.35$, with an outer radius $r_0 = 20/13$ and the inner radius $r_i = 7/13$, where the length scale is the gap D. Temperatures are fixed at T_o and $T_o + \Delta T$ at the outer and inner boundaries, respectively. The time scale is D^2/ν, and dimensionless temperatures are defined as $(T - T_o)/\Delta T$. The dimensionless temperatures on the outer/inner boundary are thus equal to 0 and 1, respectively. Magnetic induction B is scaled by $\sqrt{\rho\mu\nu_m\Omega}$, and the pressure by $\rho\nu\Omega$. Non-dimensional control parameters are the modified Rayleigh number $Ra = \alpha\, g_0\, \Delta T D/(\nu\, \Omega) = 100$, where α is the thermal expansion coefficient and g_0 the gravity at the outer radius, the Ekman number $E = \nu/(\Omega\, D^2) = 10^{-3}$ and the thermal Prandtl number $Pr = 1$. Compared to the model introduced in

section 2, the problem is solved in the frame in rotation with the spherical shell, where the no-slip conditions give a vanishing velocity on the boundaries. Because of the computational cost, we use the quasi-vacuum boundary condition $\boldsymbol{n}\times\boldsymbol{B}=\boldsymbol{0}$ on the outer radius, already used in this case by Harder and Hansen (2005). This is different from the benchmark conditions, where a potential magnetic field matching is used, which means that the obtained solution could be slightly different. As explained in Christensen et al. (2001), because non-magnetic convection is found stable against small magnetic perturbations at these parameters and because the dynamo solutions seem to have only a small basin of attraction, the initial state is of some concern. We use the same initial conditions as in Christensen et al. (2001) benchmark. In our case, the initial condition on the magnetic field has to be written for the magnetic potential. The calculation of the potential vector $\boldsymbol{A}$ reads:

$$\boldsymbol{A}=\begin{bmatrix}A_r\\A_\theta\\A_\phi\end{bmatrix}=\begin{bmatrix}\dfrac{5}{2}\ r\ \sin[\pi(r-r_i)]\cos(2\theta)+f_1(r)+\displaystyle\int(A_\theta+r\ \partial_r A_\theta)\mathrm{d}\theta\\ f_2(r,\theta)\\ \dfrac{5}{8}\left[4r_0 r-3r^2-\dfrac{r_i^4}{r^2}\right]\sin\theta+\dfrac{K}{r\sin\theta}\end{bmatrix} \tag{10}$$

with the arbitrary functions $f_1(r)$, $f_2(r,\theta)$ and the arbitrary constant K. As in Christensen et al. (2001), we define the mean magnetic energy density in the shell by

$$E_m=\frac{1}{2\ V_s\ E\ Pm}\int_{V_s}\mathbf{B}^2\mathrm{d}V \tag{11}$$

where V_s refers to the dimensionless volume of the fluid shell. The mean magnetic field strength B_{rms} used by Harder and Hansen (2005) for this benchmark is an equivalent quantity defined by $B_{rms}=\sqrt{2\ E_m}$. The dimensionless initial magnetic energy is then $E_m=868$, i.e. $B_{rms}=41.7$.

We first consider the case 0 of the benchmark, which is a non-magnetic simulation. This allows to check the validity of the thermally driven flow. The results are shown in figure 4 as a function of the spatial resolution N, defined by the third root of the number of degrees of freedom for each scalar variable, as in Matsui and Okuda (2005). We focus on the mean kinetic energy density

$$E_{kin}=\frac{1}{2\ V_s}\int_{V_s}u^2\ \mathrm{d}V \tag{12}$$

and on the drift frequency ω of the large-scale convective columns. As expected and already noticed by Matsui and Okuda (2005), the convergence is much slower with finite-element methods than with spectral methods, especially on the drift frequency. However, figure 4 shows that our results are in agreement with those of Matsui and Okuda (2005) and Harder and Hansen (2005). Both variables (E_{kin},ω) converge towards the expected values as N increases.

We now consider the case 1 of the benchmark, solving the full MHD problem. In this case, the simulations are computationally very expensive and we are limited to $N\approx 42$ with quadratic Nédélec elements. Figure 4a shows that in this case, the mean kinetic energy density is underestimated of a factor about 5%, which means that the flow is expected to be less efficient to drive a dynamo. We thus expect a dynamo threshold a bit larger than in the benchmark. Indeed, we find a dynamo threshold around $Pm\approx 7$, significantly larger than the reference value of Christensen et al. (2001) $Pm=5$. Note nevertheless that our results are coherent with those of Harder and Hansen (2005), who find an apparent slowly decaying field for $Pm=5$ (their figure 8) but a stable dynamo for $Pm=8$. The authors suggest that the slowly decaying field for $Pm=5$ corresponds to the dynamo threshold, and propose to compare the last value reached in their simulation with the benchmark value. They thus compare the mean field strength $B_{rms}\approx 42$ with the mean field strength of $B_{rms}\approx 35$ given in the benchmark. In our numerical simulation, at our dynamo threshold around $Pm\approx 7$, we obtain a mean field strength about $B_{rms}\approx 10$. Once again, this lower value is expected because our resolution underestimates the kinetic energy of the flow. With the current numerical

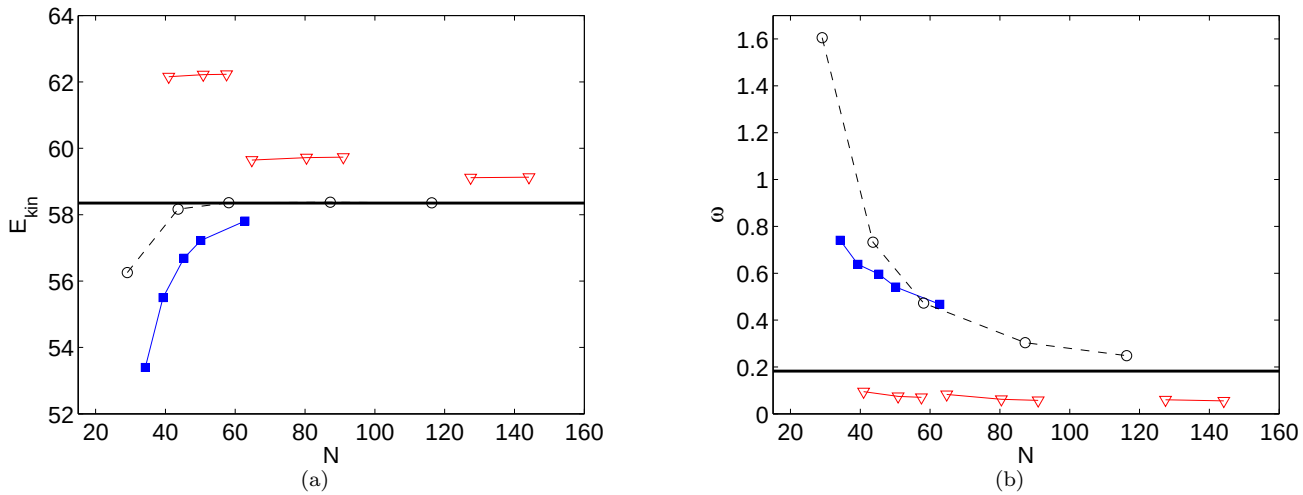

Figure 4. Evolution of (a) the kinetic energy and (b) the drift angular frequency in our numerical results (squares) for the non-magnetic case of the numerical benchmark of Christensen et al. (2001), as a function of spatial resolution N. The results are compared with the suggested solutions (continuous black line) given in Christensen et al. (2001), with the results of Harder and Hansen (2005) given by the (black) open circles, and with the numerical results of Matsui and Okuda (2005) given by the (red) triangles.

power available to us, we are not yet in a position to go any further. Nevertheless, we are convinced that the above results are encouraging towards the validation of our code to solve full dynamo problems.

4 Application to the MHD elliptical instability

The next step of our work is in the direct continuity of our previous numerical studies of the elliptical instability in non-axisymmetric geometries (Cébron et al. 2010a,b,c). We consider a triaxial ellipsoid of axes (a, b, c) with $a > b$, related to the frame (Ox, Oy, Oz), with an imposed constant tangential velocity along the deformed boundary in each plane perpendicular to the rotation axis, chosen here as the axis (Oz). Such a configuration is a model for a liquid planetary core with no solid inner core, surrounded by a solid mantle tidally deformed by a companion body. When the differential rotation between the fluid and the deformation is constant, a TDEI can be excited (see section 1), as it may be the case for the liquid core of the Early Earth (Cébron et al. 2010a, 2011). In this framework, sections 4.1 and 4.2, which respectively focus on the magnetic induction by a stationary and an unstationary mode of the TDEI, are relevant to the dynamics of the Early Earth liquid core, considering an imposed magnetic field created by an independent convective geodynamo process. When the differential rotation between the fluid and the deformation is oscillatory, a LDEI can be excited as it may be the case for the liquid core of Europa (Kerswell and Malkus 1998, Cébron et al. 2011). The case study of the magnetic induction by LDEI presented in section 4.3 could thus be related to the magnetic induction of a possibly excited LDEI in Europa considering the presence of the jovian magnetic field. Such an internal process could be of fundamental importance to correctly interpret the recorded magnetic data.

In the following, we use the mean equatorial radius $R = (a + b)/2$ as a length scale and Ω^{-1} as a time scale, where ΩR is the imposed boundary velocity at the equator. In addition to the already introduced dimensionless numbers E and Rm, two geometrical parameters are necessary to fully describe the system: the ellipticity $\beta = (a^2 - b^2)/(a^2 + b^2)$ of the elliptical deformation and the aspect ratio c/a.

4.1 *Spinover induced magnetic field*

In this section, the triaxial ellipsoid (a, b, c) is immersed into a sphere of radius $8\sqrt[3]{abc}$ containing a steady material of electrical conductivity γ_v. A constant and uniform magnetic field $\mathbf{B_0}$ is imposed parallel to the rotation axis. We focus first on the so-called spin-over mode of the elliptical instability (see figure

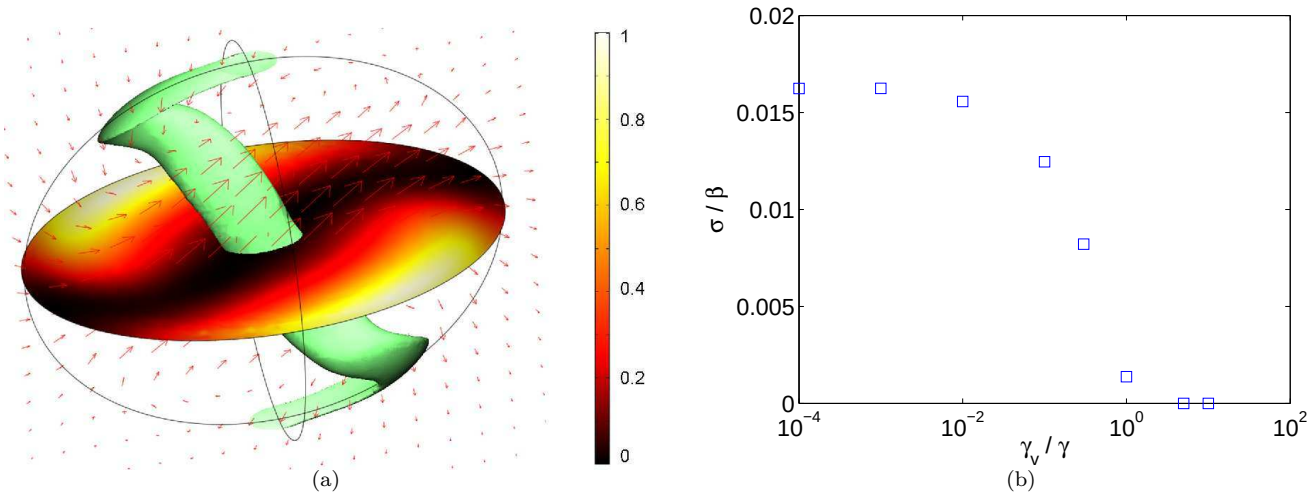

(a) (b)

Figure 5. MHD numerical simulations of the spinover mode in a triaxial ellipsoid, with an uniform magnetic field imposed along the rotation axis. The magnetic Prandtl number of the fluid is fixed to $Pm = 10^{-4}$, the ellipticity to $\beta = 0.317$ and the Elsasser number to $\Lambda = 0.02$. (a) The spinover mode is shown with an iso-surface of the velocity $||\mathbf{u}|| = 0.12$, and the induced magnetic fied is represented with arrows (the size of the arrows is proportional to the local value of the magnetic field) for $E = 1/500$. In the equatorial plane, the Joule dissipation is shown, normalized by its maximum value. (b) Evolution of the growth rate of the elliptical instability with the ratio between the outer conductivity γ_v and the fluid conductivity γ.

5a) which is obtained when the length of the polar axis is $c = (a + b)/2$ (see Cébron et al. 2010a). The magnetic Prandtl number of the fluid is fixed, $Pm = 10^{-4}$. Following Herreman et al. (2009), the magnetic field is non-dimensionalized by the magnetic scale B_0, which simply means that compared to the equations (1)-(4), the Laplace force in (1) now writes

$$\frac{\Lambda}{Rm}(\nabla \times \mathbf{B}) \times \mathbf{B_{tot}} \tag{13}$$

with $\mathbf{B_{tot}} = \mathbf{B} + (0, 0, 1)$ and where the Elsasser number associated to the imposed magnetic field is defined by $\Lambda = \gamma\, B_0^2/(\rho\Omega)$. This configuration has already been studied theoretically and experimentally in Lacaze et al. (2006), Thess and Zikanov (2007), Herreman et al. (2009) in the case of an isolating outer medium. It is explored here for the first time numerically in an ellipsoidal geometry.

A visual validation is first done on magnetic quantities, given in figure 5a, in agreement with the theoretical calculations of Lacaze et al. (2006). Figure 5b shows the influence of the outer conductivity on the growth rate of the spin-over mode. As expected, for small conductivity ratios $\gamma_v/\gamma \lesssim 10^{-3}$, the growth rate reaches a plateau as γ_v/γ decreases: the outer medium behaves as an insulating medium. Thus, in the following, we use $\gamma_v/\gamma = 10^{-4}$.

Combining the results of Lacaze et al. (2004) and Thess and Zikanov (2007), Herreman et al. (2009) proposed to model the nonlinear evolution of the spin-over mode in the laboratory frame of reference by the nonlinear system

$$\dot{\omega}_x = -\alpha_1\ (1 + \omega_z)\ \omega_y - (\nu_{so} + \Lambda/4)\ \omega_x, \tag{14}$$

$$\dot{\omega}_y = -\alpha_2\ (1 + \omega_z)\ \omega_x - (\nu_{so} + \Lambda/4)\ \omega_y, \tag{15}$$

$$\dot{\omega}_z = \beta\ \omega_x\ \omega_y - \nu_{ec}\ \omega_z + \nu_{nl}\ (\omega_x^2 + \omega_y^2) \tag{16}$$

where $\boldsymbol{\omega} = (\omega_x(t), \omega_y(t), \omega_z(t))$ is the rotation vector of the spinover mode, $\alpha_1 = \beta/(2 - \beta)$ and $\alpha_2 = \beta/(2 + \beta)$. In the limit $\beta \ll 1$, the damping terms are known analytically, as first calculated by Greenspan (1968): $\nu_{so} = \alpha\sqrt{E} = 2.62\ \sqrt{E}$ is the linear viscous damping rate of the spinover mode, $\nu_{ec} = 2.85\ \sqrt{E}$ is the linear viscous damping of axial rotation and $\nu_{nl} = 1.42\ \sqrt{E}$ is the viscous boundary layer effect on the non-linear interaction of the spinover mode with itself. The magnetic field only adds a linear term

corresponding to the Joule damping $\Lambda/4$ in the directions perpendicular to the imposed field. Even if this model does not take into account all the viscous terms of order $\sqrt{E}$ nor the non-linear corrections induced by internal shear layers (see Lacaze et al. 2004, for details), it satisfyingly agrees with experiments, regarding the growth rate as well as the non-linear saturation of the flow and induced field (Lacaze et al. 2004, Herreman et al. 2009).

Linearizing the system around the trivial fixed point $\boldsymbol{\omega} = \mathbf{0}$, the linear growth rate of the spin-over mode for $\beta \ll 1$ is given by (Herreman et al. 2009)

$$\sigma = \frac{\beta}{\sqrt{4-\beta^2}} - \tilde{\nu}_{so}, \tag{17}$$

where $\tilde{\nu}_{so} = \nu_{so} + \frac{\Lambda}{4}$. Above the instability threshold given by $\beta/\sqrt{4-\beta^2} \geq \tilde{\nu}_{so}$, a non-trivial stationary state is reached corresponding to

$$\omega_x = \pm \sqrt{\frac{\nu_{ec}\,[\sqrt{\alpha_1\alpha_2} - \tilde{\nu}_{so}]}{\alpha_2\beta - \nu_{nl}\,[\sqrt{\alpha_1\alpha_2} + \alpha_2^2/\sqrt{\alpha_1\alpha_2}]}} \approx \pm \sqrt{\frac{\nu_{ec}\,[\beta - 2\,\tilde{\nu}_{so}]}{\beta^2 - 2\,\nu_{nl}\,\beta}}, \tag{18}$$

$$\omega_y = \mp \sqrt{\frac{\nu_{ec}\,[\sqrt{\alpha_1\alpha_2} - \tilde{\nu}_{so}]}{\alpha_1\beta - \nu_{nl}\,[\sqrt{\alpha_1\alpha_2} + \alpha_1^2/\sqrt{\alpha_1\alpha_2}]}} \approx \mp \sqrt{\frac{\nu_{ec}\,[\beta - 2\,\tilde{\nu}_{so}]}{\beta^2 - 2\,\nu_{nl}\,\beta}} \approx \mp\,\omega_x, \tag{19}$$

$$\omega_z = \frac{\tilde{\nu}_{so}}{\beta}\,\sqrt{4-\beta^2} - 1 \approx \frac{2\,\tilde{\nu}_{so}}{\beta} - 1, \tag{20}$$

where approximations are done assuming $\beta \ll 1$. These expressions allow also to obtain the spin-over mode equatorial amplitude (Herreman et al. 2009):

$$\Omega_{so} = \sqrt{4\,\frac{\nu_{ec}}{\beta}\,\frac{\sigma}{\beta - 4\nu_{nl}/\sqrt{4-\beta^2}}}. \tag{21}$$

According to Lacaze et al. (2006), Herreman et al. (2009), the field induced by the non-viscous spin-over mode at low Rm is a dipole with an axis transverse to the imposed field, in quadrature with the rotation axis of the spin-over mode. The axis of length a being the long axis, the polar angle in the (x, y) plane of the saturated spin-over axis can be estimated by (Herreman et al. 2009):

$$\phi_{so} = -\left|\arctan\left[-\sqrt{\frac{2-\beta}{2+\beta}}\right]\right| \tag{22}$$

so that the vorticity of the spin-over mode is not exactly aligned with the direction of the maximum stretching at $-45°$. In the ellipsoid, the general expression of the induced field is given in Lacaze et al. (2006). In the limit of small magnetic Reynolds numbers, the cylindrical components (B_ρ, B_ϕ, B_z) of the induced magnetic field can be expressed in terms of spherical variables (r, θ, ϕ) :

$$\mathbf{B_i}(r,\theta,\phi) = Rm\;\Omega_{so}\begin{bmatrix} -\dfrac{1-r^2}{10}\sin(\phi-\phi_{so}) + \dfrac{r^2}{140}(3\;\cos(2\theta)-1)\sin(\phi-\phi_{so}) \\ \dfrac{1-r^2}{10}\cos(\phi-\phi_{so}) + \dfrac{r^2}{70}\cos(\phi-\phi_{so}) \\ -\dfrac{3\;r^2}{140}\sin(2\theta)\sin(\phi-\phi_{so}) \end{bmatrix}, \tag{23}$$

where ϕ is the polar angle in the (x, y) plane, $r = \sqrt{x^2+y^2+z^2}$ the polar radius. The induced field in the isolating outer domain is then simply given by $\mathbf{B_e} = r^{-3}\;\mathbf{B_i}(1, \theta, \phi)$.

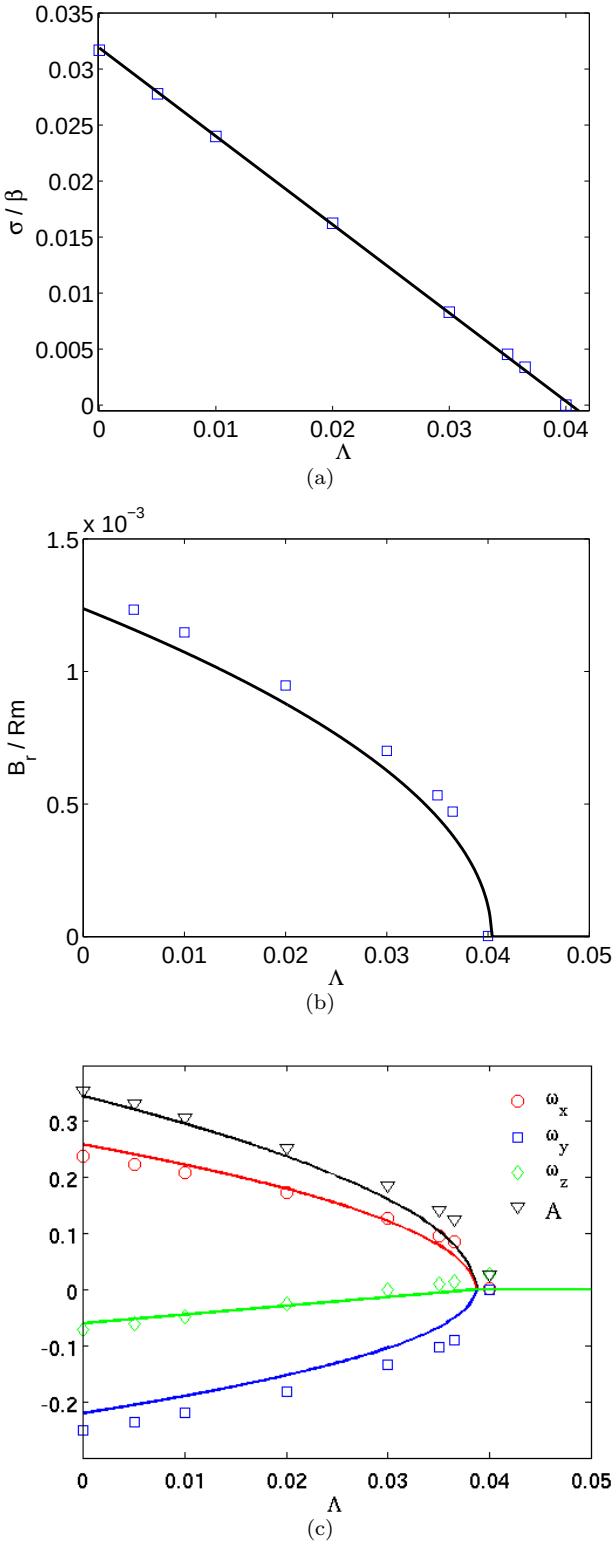

Figure 6. MHD numerical simulations (symbols) and theoretical results (continuous lines) of the spinover mode in a triaxial ellipsoid, with an uniform magnetic field imposed along the rotation axis. Parameters of the simulations are : $E = 1/344$, $\beta = 0.317$, $c = (a+b)/2$, $Pm = 10^{-4}$ for the ellipsoid of fluid, immersed into a sphere of radius 8 $\sqrt[3]{abc}$, with a conductivity $\gamma_v/\gamma = 10^{-4}$. Evolution with the Elsasser number Λ of (a) the growth rate of the elliptical instability, (b) the dimensionless amplitude of the induced radial magnetic field at the point of radius $r = 2.3$ and longitude $\phi = 45°$ in the equatorial plane ($\theta = \pi/2$) and (c) the components of the spin-over mode solid body rotation. The x-component is represented by red circles, the y-component by blue squares, the z-component by green diamonds and the amplitude $A = ||\omega||$ is given by the black triangles.

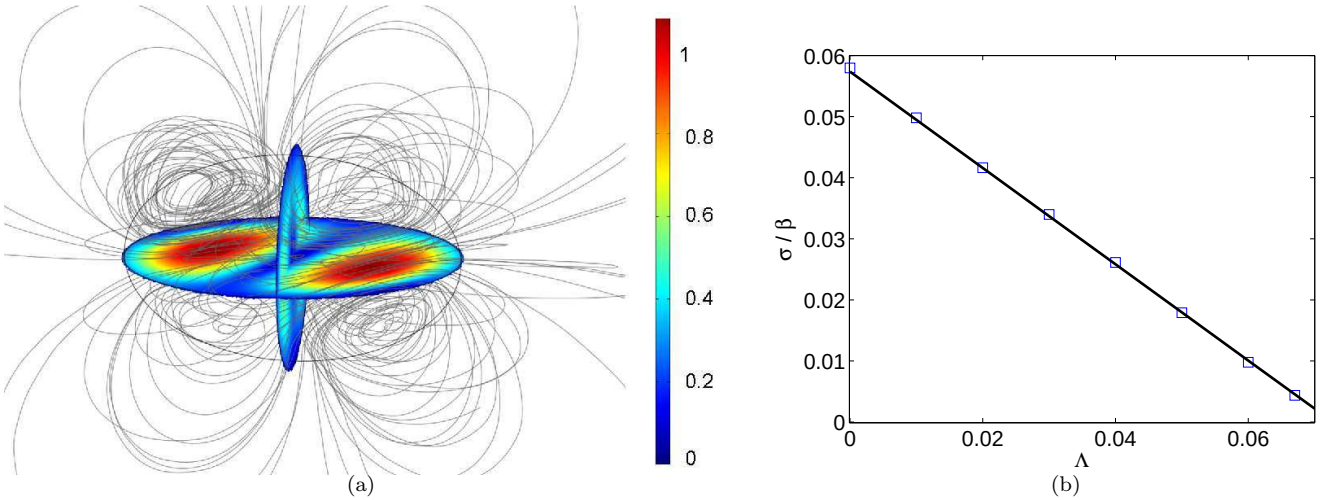

(a) (b)

Figure 7. MHD numerical simulations of the mode (1,3) of the elliptical instability in a triaxial ellipsoid, with an uniform magnetic field imposed along the rotation axis. (a) The norm of the induced magnetic field, normalized by its maximum value $B = 6.9 \cdot 10^{-4}$, is represented on slices at for the mode (1,3). Magnetic field lines are also shown. Parameters : $\beta = 0.317$, $E = 1/700$, $c/a = 0.65$ and $\Lambda = 0.02$. (b) Evolution of the growth rate of the elliptical instability with the Elsasser number Λ. The numerical simulations (blue squares) are in perfect agreement with the linear stability analysis (continuous black line) given by (24), using $\alpha = 4.24$, determined in the absence of magnetic field.

In figure 6a, the role of the Joule dissipation on the growth rate of the spin-over mode is studied, comparing the numerical results with the linear stability solution (17). The numerical growth rate is obtained as in Cébron et al. (2010a) by a best fit of the initial exponential growth of the mean amplitude of the vertical velocity $W = 1/V_s \cdot \iiint_{V_s} |w| \, \mathrm{d}V$, with w the dimensionless axial velocity and V_s the volume of the ellipsoid. The only adjusting parameter considered here is the viscous damping coefficient α, determined in the absence of magnetic field: we find $\alpha = 2.8$ rather than the theoretical value $\alpha = 2.62$, probably because of the finite value of the ellipticity β in our simulations. No adjustable coefficient is introduced for the magnetic dependence of the growth rate. The accuracy of the numerical solution is further tested on figure 6b, where the evolution of the amplitude of the radial field $\mathbf{Br}$ with the Elsasser number is compared with theoretical equation (23). We have checked that the magnetic field is radial, as expected. Finally, a last quantity of interest is the amplitude of the flow driven by the instability at saturation. Note that this quantity is not easily accessible in experiments, and was not tested in previous studies (Lacaze et al. 2006, Herreman et al. 2009). In the numerical simulations, the amplitude A of the flow driven by the instability at saturation is obtained by determining the mean additional vorticity of the flow in the bulk of the fluid (i.e. outside the viscous Ekman layers), in comparison with the imposed vorticity $2\boldsymbol{e}_z$ due to the imposed rotation. This value is then compared with the spin-over rotation vector given by (18)-(20). Results are shown in figure 6c for the three components of the spin-over mode and the amplitude $A = ||\omega||$. The excellent agreement exhibited in the three tests presented in figure 6 demonstrates that our numerical model correctly simulates both the induced field and its retroaction on the flow. We are now in a position to go further in studying induction by more complex elliptically driven flows, as relevant for planetary applications (Cébron et al. 2011). Note that these complex flows are not easily accessible to MHD theoretical or experimental approaches.

4.2 *Induced magnetic field by the mode (1,3) of the elliptical instability*

Apart from the spin-over mode, no theoretical global approach has yet been developped for other modes of the elliptical instability. Our only theoretical tool is then a WKB analysis, where perturbations of the base field are searched in the form of plane wave solutions in the limit of large wavenumbers $k \gg 1$ and for $\beta \ll 1$. Assuming a Laplace force of order β, the WKB analysis (Herreman et al. 2009, Cébron et al.

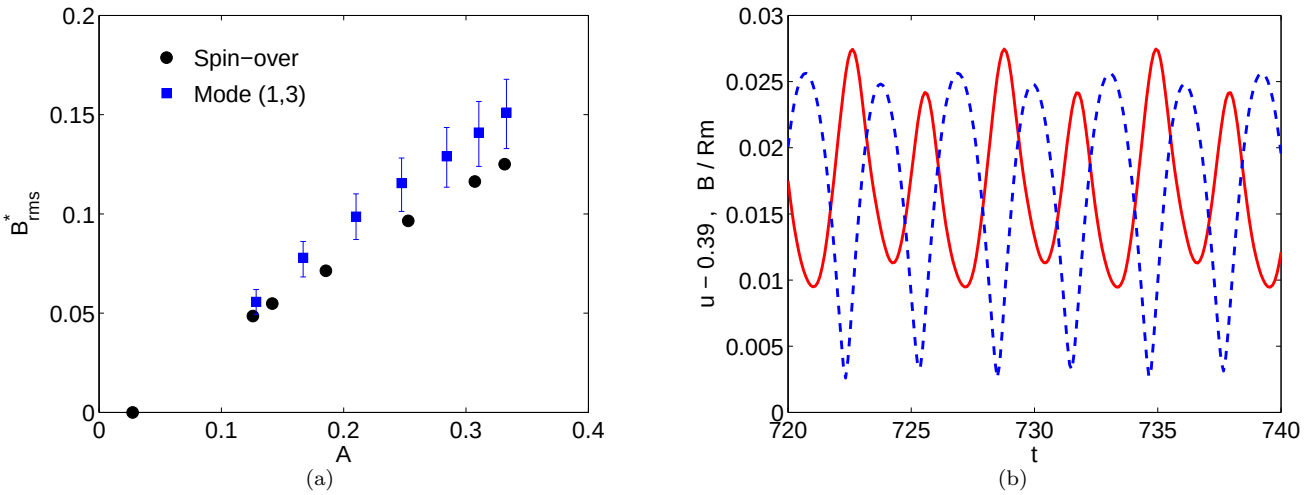

Figure 8. (a) Evolution of B^*_{rms} with the mode amplitude A. For the mode (1,3), the errorbars indicate the extrema values reached by B^*_{rms}, showing that the amplitude of the oscillations of the induced magnetic field increases with the distance to the threshold. (b) Time evolution of the velocity quantity $||\mathbf{u}|| - 0.39$ (shifted for the sake of comparison) and the magnetic field $||\mathbf{B}||/Rm$ at the point at half the long axis in the equatorial plane. The phase angle shift obtained is around 1.13, close to the expected value $\pi/2$.

2011) indicates, in the case of a stationary elliptical distortion, a growth rate

$$\sigma = \frac{9}{16}\,\beta - \alpha\sqrt{E} - \frac{\Lambda}{4}, \tag{24}$$

where α is again a viscous damping coefficient of order 1, and the induced magnetic field $\mathbf{B}$ is linked with the typical velocity of the excited mode $\mathbf{u_0}$ by:

$$\mathbf{B} = \mathrm{i}\,\frac{Rm}{2\,k}\,\mathbf{u_0}, \tag{25}$$

where k is the norm of the wave vector of the excited mode (see Cébron et al. 2011, for details). This generic expression shows that the induced magnetic field due to the elliptical instability is systematically proportional to and in quadrature with the velocity field due to the instability. Note that both solutions (24) and (25) are in agreement with the analytical results already obtained by a global method for the particular case of the spin-over mode (see section 4.1).

We validate here these results by considering the so-called $(1,3)$ mode of the elliptical instability, which is oscillating 2 times faster than the rotation rate of the flow. To do so, the length c of the ellipsoid is fixed to $c/a = 0.65$ (see Cébron et al. 2010a, for details). The typical magnetic field induced by the mode (1,3) is represented in figure 7a. In figure 7b, the excellent agreement between the theoretical and numerical growth rates of the instability confirms the general validity of the Joule damping $-\Lambda/4$. The viscous damping coefficient is found to be equal to $\alpha = 4.24$ in our simulations, which is in the expected range. The expression (25) is compared with the numerical data in figure 8a on both the spin-over mode and the mode (1,3). We defined $B^*_{rms} = 2\ k\ B_{rms}/Rm$, where B_{rms} is the quadratic mean value of the magnetic field defined by (8), $k = 2\pi/\lambda$ and where the wavelength λ is equal to $\lambda = 2$ for the spin-over mode and $\lambda = 1$ for the mode (1,3). The typical velocity u_0 corresponds to the amplitude A of the $(1,3)$ mode, which is determined by $A =< \max_V ||\mathbf{u} - \mathbf{u_b}|| >$, where the brackets indicate an average on time and $\mathbf{u_b}$ is the base flow before the destabilization of the elliptical instability. This method is less accurate than the method used in the section 4.1 for the spin-over but is more generic because it can be used for any excited mode. The collapse of the numerical induced magnetic fields B^*_{rms} for the spin-over mode and the mode (1,3) at a same distance from the threshold, and the very close values of the amplitude of the flow and the magnetic field in both cases, confirm the validity of (25). Finally in figure 8b, the phase angle shift suggested by (25) between the velocity and the induced magnetic field is validated.

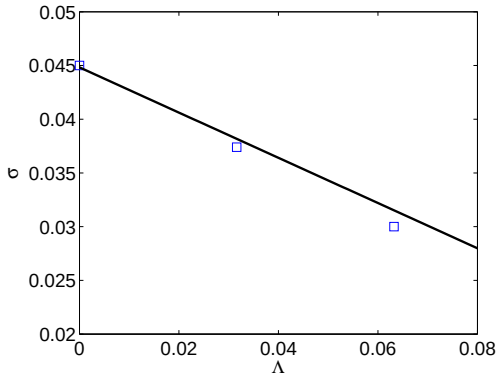

Figure 9. Evolution of the growth rate of the LDEI with the Elsasser number Λ associated to the uniform magnetic field imposed along the rotation axis for $\varepsilon = 1$, $\omega = 1.835$, $\beta = 0.44$, $c = 1$ and $E = 5 \cdot 10^{-4}$. The numerical simulations (blue squares) are in agreement with the linear stability analysis (continuous black line) given by (26), using $\alpha = 3.95$, determined in the absence of magnetic field.

4.3 *Induced magnetic field by the libration driven elliptical instability*

A recent paper by Noir et al. (2011) shows the apparition of the elliptical instability in a librating rigid triaxial ellipsoid, i.e. in the case where the whole ellipsoid is rotating at a modulated angular rate $\Omega(t) = \Omega + \Delta\phi f \sin(ft)$. Here, $\Delta\phi$ is the angular amplitude of libration in radians and f is the angular frequency of libration. Using the mean equatorial radius R as the length scale and Ω^{-1} as the time scale, the dimensionless angular rate reads $1+\varepsilon\sin(\omega t)$, with the dimensionless libration frequency $\omega = f/\Omega$ and the forcing parameter $\varepsilon = \Delta\phi\,\omega$. Note that this situation is reminiscent of the flow dynamics in the core of synchronized bodies on average, such as for instance the galilean moons Europa and Io. As demonstrated theoretically in Cébron et al. (2011), a libration driven elliptical instability (LDEI) grows in certain ranges of libration frequencies. In presence of an imposed magnetic field $\mathbf{B_0}$ parallel to the rotation axis, this analysis gives the theoretical growth rate of the LDEI in the limit of large wavenumbers $k \gg 1$ and for $\beta, \varepsilon \ll 1$

$$\sigma = \frac{16+\omega^2}{64}\,\varepsilon\beta - \alpha\sqrt{E} - \frac{\omega^2}{16}\,\Lambda, \tag{26}$$

with the Elsasser number $\Lambda = \gamma\, B_0^2/(\rho\Omega)$ and a viscous damping coefficient $\alpha \in [1;10]$. In an astrophysical context, the Joule damping term can significantly modify the stability property of the flow, and the induced field can participate in the magnetic fluctuations measured for instance in the vicinity of Europa, which is probably the most unstable of the jovian moons (Cébron et al. 2011)

Our purpose here is to validate these theoretical predictions. To do so, we use the hydrodynamic numerical model first presented in Noir et al. (2011). Note in particular that we work in the frame rotating with the ellipsoid, which leads to add the so-called Poincaré force to the Navier-Stokes equation (1). In addition to this previous study, a uniform magnetic field is imposed along the rotation axis, whereas the ellipsoid is immersed into a sphere of radius $6\ \sqrt[3]{abc}$ where the motionless medium is 10^{-4} times less electrically conductive than the fluid. As in section 4.1, we use a magnetic Prandtl number $Pm = 10^{-4}$. In order to favorize the apparition of the LDEI, we choose $\varepsilon = 1$, $\omega = 1.835$, $\beta = 0.44$, $c = 1$, and the Ekman number $E = \nu/(\Omega_0 R^2)$ is fixed at $E = 5\cdot 10^{-4}$ (see Noir et al. 2011). The expression of the growth rate (26) shows that a small Ekman number is needed to reach the threshold, because the destabilizing term $\varepsilon\beta$ is of order two. The increased computational cost imposed by the value of the Ekman number allows us to perform only three simulations, for $\Lambda = 0;\ 0.032;\ 0.063$. The excited mode of the LDEI in these simulations appears to be a spin-over mode with an oscillating direction. The obtained numerical growth rates are shown in figure 9 and confirm the validity of the Joule damping term. Concerning the magnetic field strength, at the point of radius $r = 2$ and longitude $\phi = 45°$ in the equatorial plane ($\theta = \pi/2$), already considered in figure 6b, the magnetic field is radial and equal to $B_r = 0.0013$ for $\Lambda = 0.032$, and $B_r = 0.001$ for $\Lambda = 0.063$. Considering that the theory presented in section 4.1 is still valid for this slightly oscillating

spin-over, the theoretical values obtained for the same parameters β and E are respectively $B_r = 0.0009$ and $B_r = 0.0008$, which are close to the numerical values.

4.4 *Dynamo problem*

Following our induction studies, the next step of our numerical study is to determine whether or not the elliptical instability is dynamo capable. To answer this question, and starting from an induction configuration, we can suddenly shut down the externally imposed magnetic field and report the decay/growth rate of the induced magnetic field as a function of the magnetic Reynolds number. Figure 10 shows our first numerical results. We are restricted to magnetic Reynolds numbers $Rm = Pm/E$ lower than 1000. Indeed, the mesh needed to solve higher magnetic Reynolds numbers leads to a large computational cost, up to now inaccessible. Figure 10a shows the typical dipolar decaying magnetic field for the spin-over mode. Figure 10b shows the systematic report of the decay rate for the spin-over mode and the mode (1,3), at various Ekman numbers, using an insulating outer medium (ratio of conductivities $\gamma_v/\gamma \leq 10^{-6}$). The collapse of the points along the scaling law Rm^{-1} shows that the relevant control parameter is as expected the magnetic Reynolds number. This indicates also that a purely diffusive behaviour is obtained in this range of magnetic Reynolds numbers. Note that this does not preclude a dynamo capability of the flow. Indeed, for comparison, the decay rates for a full numerical MHD simulation of a sphere precessing at an angle of 60° and a precession rate $\Omega_p = 0.3$ (which corresponds to the case studied in Tilgner 2005) are also reported for $E = 1/700$. According to Tilgner (2005), the dynamo threshold is obtained for $Pm/E \approx 7000$, at least if the role of the small inner core present in his study is negligible. The points represented in figure 10b are close to the points corresponding to elliptical instability flows and do not allow to predict such a dynamo capability. Note that these results are also close to the decay rate reported by Tilgner (1998) in his study of the kinematic dynamo ability of the Poincaré flow in a precessing spheroid of aspect ratio $c/a = 0.9$. Figure 10c is the same as figure 10b except that pseudo-vacuum conditions are used at the outer boundary. Most of the points follow the purely diffusive trend. However, the mode (1,3) seems to leave the purely diffusive behaviour for the larger Rm, which is very encouraging. Such a trend leads to expect a dynamo capability of the flow.

5 Conclusion

In conclusion, numerical simulations of dynamo are tractable with the commercial software COMSOL Multiphysics®, based on a finite-element method. Successfull validations have been obtained for kinematic dynamos on a Ponomarenko-like problem and a Von Karman flow, and also on the thermally driven dynamic dynamo of the Christensen et al. (2001) benchmark. This finite element approach presents the great advantage of being capable of dealing easily with complex geometries. In the present study, we have focused on the MHD flows in a triaxial ellipsoid, representative of a tidally deformed planetary core. The first MHD numerical simulations of the elliptical instability under an imposed magnetic field in this geometry have been presented. Results regarding the instability growth rate in the presence of Joule dissipation and the induced magnetic field have been discussed, and the analytical results coming from local studies have been confirmed. In the near future, following the parallelization of the software COMSOL Multiphysics® and the resulting increased computational power, it is expected that the elliptical instability will be validated as a dynamo capable forcing at the planetary scale.

6 Acknowledgments

The authors are grateful to C. Nore (LIMSI, Orsay) for fruitful discussions.

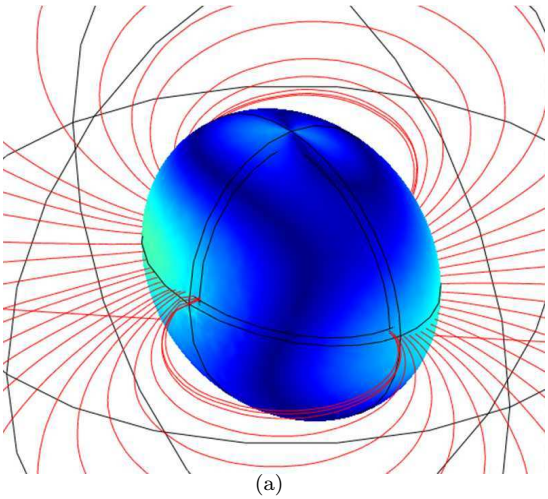

(a)

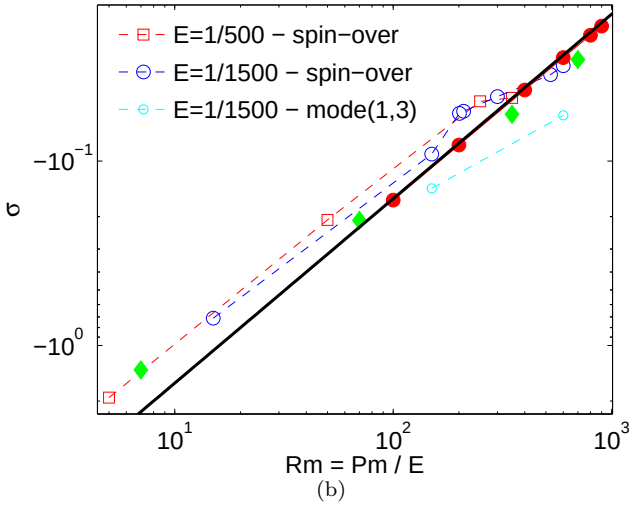

(b)

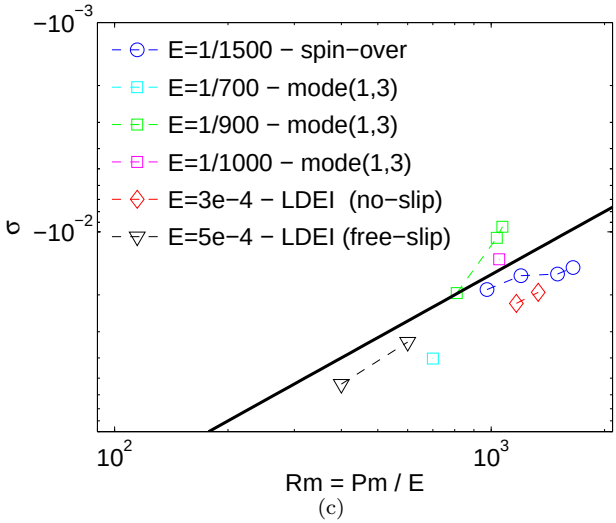

(c)

Figure 10. Decaying magnetic field once the external imposed magnetic field is shut down. (a) The norm of the cylindrical outward radial component of the magnetic field (normalized by its maximum value) is represented at the outer boundary of the ellipsoidal fluid domain. This decaying field is obtained for the spin-over mode at the parameters $\beta = 0.317$, $E = 1/500$, $c = (a+b)/2$ and $Rm = 500$. (b) The fluid ellipsoid is immersed into a sphere of radius $10\ \sqrt[3]{abc}$ with an electrical conductivity 10^{-4} smaller than the conductivity of the fluid. The figure shows the result for the elliptical instability (open symbols) and for the precession case (solid symbols). The black continuous line stands for the scaling law $-16/Rm$, i.e. a purely diffusive behaviour. The results of Tilgner (1998) are represented by red circles whereas the green diamonds are the numerical results of our full MHD simulations of a sphere precessing at an angle of 60°, a precession rate $\Omega_p = 0.3$ and $E = 1/700$. (c) Same as figure (b) but with pseudo-vacuum conditions at the outer boundary. For comparison, some simulations with the LDEI flow are also reported in the case of no-slip boundaries, for $\varepsilon = 0.92$, $\omega = 1.76$, $\beta = 0.44$, $c = 1$ and $E = 5 \cdot 10^{-4}$; and in the case of free-slip boundaries for $\varepsilon = 1$, $\omega = 1.8$, $\beta = 0.44$, $c = 1$ and $E = 3 \cdot 10^{-4}$.

REFERENCES

Bossavit, A., 1988. A rationale for edge-elements in 3-D fields computations. IEEE Trans. Magn. 24, 74-79.

Bossavit, A., 1990. Solving Maxwell's equations in a closed cavity, and the question of spurious modes. IEEE Trans. Magn. 26, 702-705.

Busse, F. H., 2002 Convective flows in rapidly rotating spheres and their dynamo action. Phys. Fluids, 14, 1301-1314.

Cébron, D., Le Bars, M., Leontini, J., Maubert, P., Le Gal, P., 2010a. A systematic numerical study of the elliptical instability in a rotating triaxial ellipsoid. Phys. Earth Planet. Int., 182, 119-128.

Cébron, D., Maubert, P., Le Bars, M., 2010b. Tidal instability in a rotating and differentially heated ellipsoidal shell. Geophys. J. Int., 182, 1311-1318.

Cébron, D., Le Bars, M., Meunier, M., 2010c. Tilt-over mode in a precessing triaxial ellipsoid. Phys. Fluids, 22, 116601.

Cébron, D., Le Bars, M., Moutou, C., Maubert, P., Le Gal, P., 2011. Elliptical instability in terrestrial planets & moons. Submitted to A & A.

Chan, K. H, Zhang, K., Liao, X., 2010. An EBE finite element method for simulating nonlinear flows in rotating spheroidal cavities. Int. J. Num. Meth. Fluids, 63, 3, pp. 395 - 414.

Chan, K. H., K. Zhang, J. Zou, and G. Schubert (2001), A non-linear, 3-D spherical α^2 dynamo using a finite element method, Phys. Earth Planet. Int., 128, 35-50.

Costabel, M., 1991. A coercive bilinear form for Maxwell's equations. Journal of mathematical analysis and applications, 157, 2, 527–541.

Clune, T.C., Elliot, J.R., Miesch, M., Toomre, J., Glatzmaier, G.A., 1999. Computational aspects of a code to study rotating turbulent convection in spherical shells. Parallel Comput. 25, 361-380.

Christensen, U.R., Aubert, J., Cardin, P., Dormy, E. and Gibbons, S., Glatzmaier, G.A., Grote, E. and Honkura, Y., Jones, C., Kono, M. and others, 2001. A numerical dynamo benchmark. Phys. Earth Planet. Int., 128, 1–4, pp. 25–34.

Donati, J.F., Moutou, C., Farès, R., Bohlender, D., Catala, C. and Deleuil, M., Shkolnik, E., Cameron, A.C., Jardine, M.M. and Walker, G.A.H., 2008. Magnetic cycles of the planet-hosting star τ Bootis. M.N.R.A.S., 385, 3, pp. 1179–1185.

Dormy, E., Valet, J.P., Courtillot, V., 2000. Numerical models of the geodynamo and observational constraints. Geochem. Geophys. Geosyst, 1, 10, 1037.

Fares, R., Donati, J.F., Moutou, C., Bohlender, D., Catala, C. and Deleuil, M., Shkolnik, E., Cameron, A.C., Jardine, M.M. and Walker, G.A.H., 2009. Magnetic cycles of the planet-hosting star τ Bootis–II. A second magnetic polarity reversal. M.N.R.A.S., 398, 3, pp. 1383–1391.

Fournier, A., Bunge, H.-P., Hollerbach, R., and Vilotte, J.-P., 2004. Application of the spectral-element method to the axisymmetric navier-stokes equation. Geophys. J. Int., 156, 682-700.

Fournier, A., Bunge, H.-P., Hollerbach, R., and Vilotte, J.-P., 2005. A Fourier-spectral element algorithm for thermal convection in rotating axisymmetric containers. Journal of Computational Physics, 204, 2, 462-489.

Gissinger, C. J. P., 2009. A numerical model of the VKS experiment. EPL, 87, 39002.

Glatzmaier, G.A. & Roberts, P.H, 1995. A three-dimensional self-consistent computer simulation of a geomagnetic field reversal. Nature 377, 203-209.

Greenspan, H. P., 1968. The Theory of Rotating Fluids, Cambridge University Press, Cambridge.

Guermond, J.L., Laguerre, R., Léorat, J. and Nore, C., 2007. An interior penalty Galerkin method for the MHD equations in heterogeneous domains.Journal of Computational Physics, 221, 1, 349–369.

Harder, H., Hansen, U., 2005. A finite-volume solution method for thermal convection and dynamo problems in spherical shells. Geophys. J. Int., 161, 522–532.

Hejda, P. and Reshetnyak, M., 2003. Control Volume Method for the Dynamo Problem in the Sphere with the Free Rotating Inner Core. Stud. Geophys. Geod., 47, 147-159.

Hejda, P. and Reshetnyak, M., 2004. Control volume method for thermal convection problem in a rotating spherical shell: test on the benchmark solution, Stud. Geophys. Geod., 48, 741-746.

Herreman, W., Le Bars, M., Le Gal, P., 2009. On the effects of an imposed magnetic field on the elliptical instability in rotating spheroids. Phys. Fluids 21, 046602.

Herreman, W., Cebron, D., Le Dizès, S. Le Gal, P., 2010. Elliptical instability in rotating cylinders: liquid metal experiments under imposed magnetic field. J. Fluid Mech., 661, pp 130-158.

Hesthaven, JS and Warburton, T., 2004: High–order nodal discontinuous Galerkin methods for the Maxwell eigenvalue problem. Phil. Trans. Roy. Soc. London. Series A: Mathematical, Physical and Engineering Sciences. Vol. 362, 1816, pp. 493.

Hindmarsh, A. C., Brown, P. N., Grant, K. E., Lee, S. L., Serban, R., Shumaker, D. E., Woodward, C. S., 2005. SUNDIALS: Suite of Nonlinear and Differential/Algebraic Equation Solvers. ACM T. Math. Software, 31, p. 363.

Iskakov, A. B., Descombes, S., Dormy, EM., 2004. An integro-differential formulation for magnetic induction in bounded domains: boundary element-finite volume method. J. Comput. Phys. 197 (2), 540-554.

Jiang, B.N., Wu, J. and Povinelli, L.A., 1996. The origin of spurious solutions in computational electromagnetics. J. Comput. Phys. 125, 1, 104–123.

Jin, J. M., 1993. The finite element method in electromagnetics. Wiley.

Jones, C.A., 2003. Dynamos in planets. Stellar Astrophysical Fluid Dynamics, 1, 159–176.

Jones, C.A., 2011. Planetary and Stellar Magnetic Fields and Fluid Dynamos. Annu. Rev. Fluid Mech., 43, 1.

Kageyama, A. and Sato, T., 1997. Velocity and magnetic field structures in a magnetohydrodynamic dynamo, Phys. Plasma, 4(5), 1569-1575.

Kaiser, R., and Tilgner, A., 1999. Kinematic dynamos surrounded by a stationary conductor. Phys. Rev. E 60, 2949.

Kerswell, R. R., 1996. Upper bounds on the energy dissipation in turbulent precession. J. Fluid Mech., 321, 335-370.

Kerswell, R. R., 2002. Elliptical instability. Annu. Rev. Fluid Mech., 34, 83–113.

Kerswell, R. R., Malkus, W. V. R., 1998. Tidal instability as the source for Io's magnetic signature. Geophys. Res. Lett. 25, 603–6.

Lacaze, L., Le Gal, P., Le Dizès, S., 2004. Elliptical instability in a rotating spheroid. J. Fluid Mech. 505, 1–22.

Lacaze, L., Herreman, W., Le Bars, M., Le Dizès, S., Le Gal, P., 2006. Magnetic field induced by elliptical instability in a rotating spheroid. Geophys. Astrophys. Fluid Dyn. 100, 299–317.

Laguerre, R.., 2006. Approximation des équations 3D de la magnétohydrodynamique par une méthode spectrale-éléments finis nodaux. Compte-rendus des Rencontres du Non-Linéaires.

Loper, D.E., 1975. Torque balance and energy budget for the precessionally driven dynamo. Phys. Earth. Planet. Inter. 11, 43-60.

Malkus, W. V. R., 1968, Precession of the earth as the cause of geomagnetism. Science, 160, 259–264.

Nédélec, J. C., 1980. Mixed finite elements in R3 . Numer. Math., 35, 315-341.

Nédélec, J. C., 1986. A new family of mixed finite elements in R3 . Numer. Math. 50, 57-81.

Manglik, A., Wicht, J., Christensen, U. R., 2010. A dynamo model with double diffusive convection for Mercury's core . Earth and

Planetary Science Letters, Volume 289,s 3-4, pp. 619-628.
Matsui, H., Okuda, H., 2004. Development of a simulation code for MHD dynamo processes using the GeoFEM platform, Int. J. Comput. Fluid. D.,18, pp.323-332.
Matsui, H., Okuda, H., 2005. MHD dynamo simulation using the GeoFEM platform - verification by the dynamo benchmark test. Int. J. Comput. Fluid Dyn., 19, 15-22.
Monk, P., 2003. Finite Element Methods for Maxwell's Equations. Oxford University Press.
Noir, J., Cebron, D., Le Bars, M., Aurnou, J. M., 2011.Zonal flow and elliptical instability in librating non-axisymmetric containers. Submitted to Phys. Earth Planet.Int.
Paulsen, K. D., and Lynch, D. R. Elimination of vector parasites in finite element Maxwell solutions. IEEE Trans. Microwave Theo. Tech., 39:395-404, 1991.
Ponomarenko, Y. B., 1973. Theory of the hydromagnetic generator. Journal of Applied Mechanics and Technical Physics, Vol. 14, Number 6, 775-778.
Rieutord, M., 2008. The solar dynamo. Comptes Rendus Physique, Volume 9, 7, pp. 757-765.
Rochester, M.G., Jacobs, J.A., Smylie, D.E. and Chong, K.F. 1975. Can precession power the geomagnetic dynamo? Geophys. J . R. Astron. Soc. 43, 661-678.
Sun, D., Manges, J., Yuan, X. and Cendes, Z., 1995. Spurious modes in finite-element methods. Antennas and Propagation Magazine, IEEE, 37, 5, 12–24.
Thess, A., Zikanov, O., 2007. Transition from two-dimensional to three-dimensional magnetohydrodynamic turbulence. J. Fluid Mech., 579, p. 383-412.
Tilgner, A., 1998. On Models of Precession Driven Core Flow. Studia Geophysica et Geodaetica, 42, 3, 232–238.
Tilgner, A., 2005. Precession driven dynamos. Phys. Fluids 17, 034104.
Volakis, J. L., Chatterjee, A. and Kempel, L. 1998 Finite element methods for electromagnetics: antennas, microwave circuits and scattering applications. New York: IEEE Press.
Wicht, J., Tilgner, A., 2010. Theory and Modeling of Planetary Dynamos. Space Science Reviews, Volume 152, Numbers 1-4, 501-542.
Wu, C. C. and Roberts, P. H., 2009. On a dynamo driven by topographic precession. Geophys. Astrophys. Fluid Dyn. 103, 467-501.